Monthly Notices of the ROYAL ASTRONOMICAL SOCIETY

MNRAS **517,** 2867–2875 (2022) https://doi.org/10.1093/mnras/stac2837
Advance Access publication 2022 October 4

The white dwarf binary pathways survey – VIII. A post-common envelope binary with a massive white dwarf and an active G-type secondary star

M. S. Hernandez [1,2]★ M. R. Schreiber,[1,2]★ S. G. Parsons [3] B. T. Gänsicke [4,5] O. Toloza,[1,2] M. Zorotovic,[6] R. Raddi [7] A. Rebassa-Mansergas[7,8] and J. J. Ren [9]

[1]*Departamento de Física, Universidad Técnica Federico Santa María, Av. España 1680, Valparaíso, Chile*
[2]*Millennium Nucleus for Planet Formation, NPF, Av. España 1680, Valparaíso, Chile*
[3]*Department of Physics and Astronomy, University of Sheffield, Sheffield S3 7RH, UK*
[4]*Department of Physics, University of Warwick, Gibbet Hill Road, Coventry, CV4 7AL, UK*
[5]*Centre for Exoplanets and Habitability, University of Warwick, Coventry CV4 7AL, UK*
[6]*Instituto de Física y Astronomía de la Universidad de Valparaíso, Av. Gran Bretaña 1111, Valparaíso, Chile*
[7]*Departament de Física, Universitat Politècnica de Catalunya, c/Esteve Terrades 5, E-08860 Castelldefels, Spain*
[8]*Institute for Space Studies of Catalonia, c/Gran Capità 2-4, Edif. Nexus 201, E-08034 Barcelona, Spain*
[9]*Key Laboratory of Space Astronomy and Technology, National Astronomical Observatories, Chinese Academy of Sciences, Beijing 100101, P. R. China*

Accepted 2022 September 30. Received 2022 September 29; in original form 2022 June 29

ABSTRACT

The white dwarf binary pathways survey is dedicated to studying the origin and evolution of binaries containing a white dwarf and an intermediate-mass secondary star of the spectral type A, F, G, or K (WD + AFGK). Here, we present CPD-65 264, a new post-common envelope binary with an orbital period of 1.37 d that contains a massive white dwarf ($0.86 \pm 0.06\,M_{\odot}$) and an intermediate-mass ($1.00 \pm 0.05\,M_{\odot}$) main-sequence secondary star. We characterized the secondary star and measured the orbital period using high-resolution optical spectroscopy. The white dwarf parameters are determined from *HST* spectroscopy. In addition, *TESS* observations revealed that up to 19 per cent of the surface of the secondary is covered with starspots. Small period changes found in the light curve indicate that the secondary is the second example of a G-type secondary star in a post-common envelope binary with latitudinal differential rotation. Given the relatively large mass of the white dwarf and the short orbital period, future mass transfer will be dynamically and thermally stable and the system will evolve into a cataclysmic variable. The formation of the system can be understood assuming common envelope evolution without contributions from energy sources besides orbital energy. CPD-65 264 is the seventh post-common envelope binaries with intermediate-mass secondaries that can be understood assuming a small efficiency in the common envelope energy equation, in agreement with findings for post-common envelope binaries with M-dwarf or substellar companions.

Key words: stars: activity – binaries: close – stars: solar-type – white dwarfs.

1 INTRODUCTION

Close binary stars containing at least one white dwarf are important for a wide variety of astrophysical contexts ranging from understanding the occurrence rates and delay time distributions of SN Ia explosions (e.g. Mennekens et al. 2010) to characterizing the low frequency gravitational wave background (e.g. Korol et al. 2017). Despite this importance, we still do not fully understand the formation and evolution of these fascinating objects.

The formation of most white dwarf binaries with periods shorter than a few weeks is thought to be caused by common envelope evolution (Paczynski 1976; Webbink 1984). Indeed, the distributions of these close white dwarf binaries with M-dwarf (Zorotovic et al. 2010; Camacho et al. 2014) or substellar companions (Lagos et al. 2021; Zorotovic & Schreiber 2022) can be well reproduced by simple prescriptions of common envelope evolution.

The situation is more complex when the initial main-sequence binary consists of two stars with masses $\gtrsim 1M_{\odot}$. Such binaries are the progenitors of close white dwarf binaries with secondary stars $\gtrsim 1M_{\odot}$ as well as of close double white dwarfs. It seems that for these populations, models based on common envelope evolution alone are unable to reproduce the characteristics of observed samples (e.g. Nelemans et al. 2000). Instead at least two evolutionary channels, i.e. common envelope evolution and stable but non-conservative mass transfer seem to be required to explain the observed populations in both cases (Webbink 2008; Woods et al. 2012; Lagos et al. 2022). In addition, at least one system (IK Peg) can only be understood as a post-common envelope binary if energy sources in addition to orbital energy contribute during the common envelope phase. Interestingly, IK Peg contains a massive white dwarf ($1.19\,M_{\odot}$) and it has therefore been suggested that if mass transfer starts when a relatively massive donor star is close to the tip of the asymptotic giant branch (AGB), recombination energy might play an important role (Rebassa-Mansergas et al. 2012b).

However, the currently available observed samples of both close double white dwarfs (e.g. Napiwotzki et al. 2020; Schreiber et al. 2022) and close white dwarf with F or G type companions (Lagos

★ E-mail: mercedes.hernandez@postgrado.uv.cl (MSH); matthias.schreiber@usm.cl (MRS)

et al. 2022) are rather small and/or heavily affected by selection effects. In particular, IK Peg remains the only systems containing a relatively massive white dwarf (exceeding 0.8 $M_\odot$) and it therefore remains unclear whether other energy sources during common envelope evolution need to be considered for all post-common envelope binaries that contain massive white dwarfs or if IK Peg is perhaps just an outlier and the overall population of post-common envelope binaries can be understood considering only orbital energy during common envelope evolution. To progress with this situation, we are currently performing a large-scale survey of white dwarfs with close intermediate-mass companions $\gtrsim$ 1 $M_\odot$ *The White Dwarf Binary Pathways Survey*.

Finding white dwarfs in close binary systems is relatively simple if the companion is of a substellar class or a low-mass main-sequence (spectral type M) star (Rebassa-Mansergas et al. 2010, 2016). However, when the companion to the white dwarf is of spectral type A, F, G, or early-K, the latter completely outshines the white dwarf at optical wavelengths which makes finding these objects in spectroscopic surveys difficult. To overcome this problem, we combined optical (e.g. The Radial Velocity Experiment-RAVE; Kordopatis et al. 2013) and ultraviolet observations (Galaxy Evolution Explorer-*GALEX*; Bianchi 2014), to select main-sequence stars with an excess at ultraviolet wavelengths which is indicative for the presence of a white dwarf companion star (Parsons et al. 2016; Rebassa-Mansergas et al. 2017).

Here, we present a detailed characterization of CPD-65 264, a white dwarf with a G-type secondary star in a close orbit (1.37 d). The system can be understood as a post-common envelope binary that did not require any additional energy (apart from orbital energy) to expel the envelope of the giant and that simply will evolve into a cataclysmic variable in the future. This system increases the number of known post-common envelope binaries with intermediate-mass secondaries to seven (Parsons et al. 2015; Hernandez et al. 2021, 2022). Among the systems discovered by our survey, CPD-65 264 contains the most massive white dwarf (0.86 $M_\odot$). The large mass of the white dwarf in CPD-65 264 implies that the progenitor of the white dwarf had evolved to late stages on the AGB when the mass transfer started that led to common envelope evolution. As shown by Rebassa-Mansergas et al. (2012b, their fig. 6), post-common envelope binaries containing white dwarf masses exceeding $\sim$0.8 $M_\odot$ are the most suitable targets to test common envelope theories because already at relatively short periods ($\lesssim 3-4$ d depending somewhat on the secondary star mass) these systems would provide evidence for extra energy sources contributing to common envelope evolution. The fact that the period of CPD-65 264 is well below this threshold further indicates that in the vast majority of cases orbital energy is sufficient to explain the observed properties of post-common envelope binaries. Perhaps, only for post-common envelope binaries with very large white dwarf masses, exceeding 1 $M_\odot$ such as the white dwarf in IK Peg, recombination energy becomes important.

Using the available *Transiting Exoplanet Survey Satellite* (*TESS*; Ricker et al. 2015) data, we also find the secondary star to be differentially rotating and very active (spots cover 8–19 per cent of its surface). As we have observed similar patterns in two post-common envelope binaries previously characterized by our survey, differential rotation seems to rather frequently occur in rapidly rotating G-type stars. *TESS* light curves of post-common envelope binaries can therefore be used to study activity in the fast rotation regime.

2 OBSERVATIONS

We used optical high-resolution spectroscopy to determine the orbital period of the system and to characterize the secondary star. *HST* far-ultraviolet spectroscopy was used to measure the white dwarf parameters. In what follows, we briefly describe the observational setups and data reduction tools that we utilized to study CPD-65 264.

2.1 High-resolution optical spectroscopy

We carried out time-resolved high-resolution optical spectroscopic follow-up observations to confirm the close binarity of CPD-65 264 by measuring the radial velocity variations. We used the Ultraviolet and Visual Echelle Spectrograph (UVES; Dekker et al. 2000) on the ESO-VLT and the Fiber-fed Extended Range Optical Spectrograph (FEROS; Kaufer et al. 1999) at the 2.2 m-MPG telescope. The observations carried out with UVES have a spectral resolution of 58 000 for a 0.7-arcsec slit. With its two-arms, UVES covers the wavelength range of 3000–5000 Å (blue) and 4200–11 000 Å (red), centred at 3900 and 5640 Å, respectively. Standard data reduction was performed using the specialized pipeline ESOREFLEX workflow (Freudling et al. 2013). The data obtained with FEROS have a resolution of $R \approx 48\,000$ and covers the wavelength range from $\sim$3500 to 9200 Å. The spectra were extracted and analysed with the CERES code (Jordán et al. 2014; Brahm, Jordán & Espinoza 2017), an automated pipeline developed to process spectra coming from different instruments in an homogeneous and robust manner following the procedures described in Marsh (1989). The instrumental drift in wavelength through the night was corrected with a secondary fiber observing a Th-Ar lamp.

2.2 *HST* spectroscopy

With the purpose of confirming the presence of the white dwarf and measuring its mass, we performed far-ultraviolet spectroscopic observations with the Space Telescope Imaging Spectrograph (STIS; Kimble et al. 1998) onboard of the *HST*. The observation was carried out on 2021 April 21 as part of the program N^{o} 16224 over a single spacecraft orbit resulting in a spectrum with a total exposure time of 2526 s. We used the MAMA detector and the G140L grating providing a spectral resolution between 960 and 1440 over the wavelength range of 1150–1730 Å. The far-ultraviolet spectrum was extracted and wavelength calibrated following the standard procedures on the STIS pipeline (Sohn et al. 2019).

3 BINARY AND STELLAR PARAMETERS

In this section, we describe how we use the above described observations to determine the binary and stellar parameters of the system.

3.1 Orbital period

The first step to obtain the orbital period is to calculate the radial velocities from the high-resolution spectra. For the UVES spectra we used the cross-correlation technique against a binary mask representative of a G-type star. The uncertainties in radial velocity were computed using scaling relations (Jordán et al. 2014) with the signal-to-noise ratio and width of the cross-correlation peak, which was calibrated with Monte Carlo simulations. Radial velocities from FEROS spectra were obtained during data processing with the CERES code that also calculates radial velocities using cross-correlation. A total of 15 spectra were analysed, the entire list of measured radial velocities can be found in Table 1. The statistical uncertainties of the radial velocities derived from the UVES data are slightly larger than those derived from FEROS because the weather conditions were

Table 1. CPD-65 264 radial velocity measurements. The given uncertainties are purely statistical.

Instrument	BJD	RV (km s^{-1})	Error (km s^{-1})
FEROS	2457000.73641	6.92	0.08
FEROS	2457001.73740	− 78.53	0.13
FEROS	2457002.73840	55.30	0.10
FEROS	2457003.54079	36.24	0.08
FEROS	2457003.62190	71.67	0.09
FEROS	2457003.67652	91.36	0.08
FEROS	2457003.73820	107.96	0.09
FEROS	2457003.79036	116.33	0.09
FEROS	2457004.53880	− 81.35	0.19
FEROS	2457004.69224	− 55.47	0.09
FEROS	2457004.75222	− 34.29	0.10
FEROS	2457004.80855	− 10.69	0.12
FEROS	2457383.58068	103.14	0.08
UVES	2458231.49972	63.35	0.29
UVES	2458352.87197	− 56.65	0.71

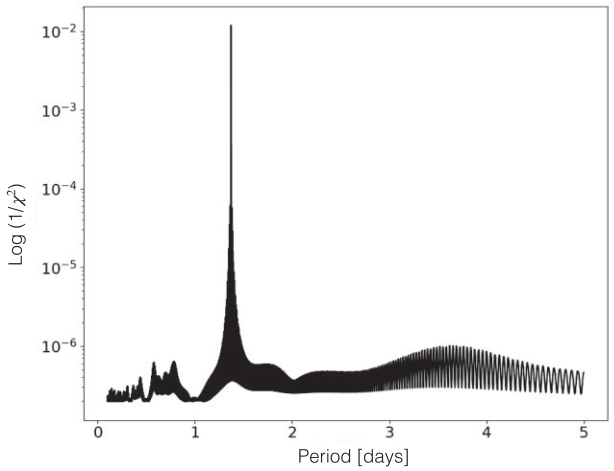

Figure 1. Periodogram of the radial velocity measurements of CPD-65 264. The highest peak corresponds to the orbital period of the system. The fit provides a χ^2 of 104.8 and a reduced χ^2 of 8.7. This relatively large value indicates that systematic errors slightly dominate the purely statistical uncertainties of our radial velocity measurements.

slightly worse which translated to a slightly lower signal-to-noise ratio.

We used the radial velocities to calculate the orbital period following a least-squares spectral analysis, i.e. we fitted the measurements with a sinusoid of a range of periods and determined χ^2. The highest peak (smallest χ^2) in Fig. 1 provides the orbital period of 1.3704 d. The phase-folded radial velocity curve is shown in Fig. 2 and clearly illustrates the overall agreement of the fit with the data. Inspecting the residuals, however, we note that the scatter of the measurements around the model solution is larger than expected from the statistical uncertainties of our radial velocity measurements. This is in agreement with the relatively large reduced χ^2 of 8.7 we obtained from the sinosoidal fit and indicates that the statistical errors of our radial velocity measurements significantly underestimate the true uncertainties, i.e. systematic errors dominate the radial velocity measurements. We used the scatter around the sinosoidal fit to estimate the systematic error and obtained 1.93 km s^{-1} (standard deviation). As discussed in Parsons et al. (2015), this systematic radial

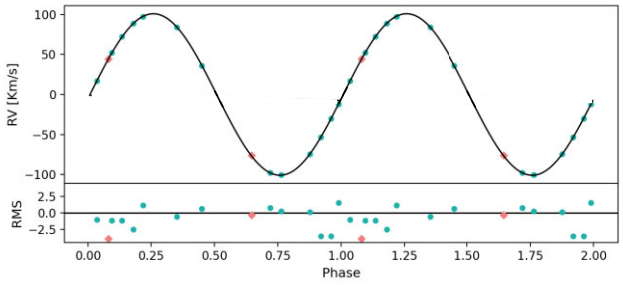

Figure 2. Radial velocity curve of CPD-65 264 phase folded over the orbital period of 1.37 d. Radial velocities measurements derived from spectra taken with FEROS are represented with the green dots, while the red diamonds represent radial velocities measured from UVES spectra. The residuals exceed what is expected from the very small statistical uncertainties and indicate that a systematic error of the order of ∼1.93 km s^{-1} dominates.

velocity uncertainty is likely due to the main-sequence star's large rotational broadening causing small systematic errors during the cross-correlation process. For completeness, we note that performing the period determination with the larger systematic uncertainties leads to exactly the same results (except of an unimportant increase of the uncertainty of the measured orbital period).

3.2 The secondary star

We adopted the method described in Hernandez et al. (2022) to measure the stellar parameters of the main-sequence star. The procedure is divided in two steps. First, we determined the initial values for effective temperature ($T_{\rm eff}$), surface gravity ($\log g$), metallicity (Z), and rotational broadening ($v \sin i$), by normalizing one of the FEROS spectra and fit it with MARCS.GES[1] models (Gustafsson et al. 2008) using iSpec (Blanco-Cuaresma et al. 2014). We started off this spectral fit at the values delivered by the CERES pipeline, i.e. $T_{\rm eff} = 5800$ K, $\log g = 4.5$ dex, $v \sin i = 50$ km s^{-1}, and solar metallicity, but also performed fits with the initial values perturbed by $T_{\rm eff}$ ±100 K, $\log g$ ±0.5 dex, $v \sin i$ ±10 km s^{-1}, and Z ±0.5 dex. The procedure always converged to the same best fit.

Second, we created a spectral energy distribution (SED) using the *Gaia* EDR3 (Gaia Collaboration 2020) $G_{\rm BP}$, $G_{\rm RP}$, and G magnitudes, along with J, H, and Ks band data from the Two Micron All-Sky Survey (2MASS; Cutri et al. 2003), and $W1$ and $W2$ band data from Wide-field Infrared Survey Explorer (*WISE*; Cutri et al. 2012) and complemented this information with the parallax (4.85 ± 0.01 mas) and reddening ($E(B-V) = 0.060 \pm 0.005$ mag) which are provided by *Gaia* EDR3 and the STILISM reddening map[2] (Capitanio et al. 2017; Lallement et al. 2019), respectively. We then fitted the SED taking into account reddening and parallax using the Markov chain Monte Carlo (MCMC) method (Press et al. 2007) to determine the final values of mass, radius, effective temperature, and surface gravity with their corresponding uncertainties. As initial parameters, we used the effective temperature and surface gravity previously obtained in step one while the radius was initialized at a value for a main-sequence star with the corresponding $\log g$ and $T_{\rm eff}$. The resulting values with their uncertainties are listed in Table 2. The obtained SED is presented in Fig. 3.

[1] https://marcs.astro.uu.se/
[2] https://stilism.obspm.fr/

Table 2. Summary of the binary and individual stellar parameters of the CPD-65 264. All uncertainties are purely statistical except of those of the white dwarf parameters which are rough estimates of the dominating systematic errors.

Parameter	CPD-65 264
m_V (mag)	11.17 ± 0.09
Orbital period (d)	1.3704 ± 0.0001
Phase zero (BJD)	2457004.874 ± 0.007
a ($R_\odot$)	6.44 ± 0.01
Distance (pc)	206.01 ± 0.47
Inclination (deg)	64 ± 1
Sec. amplitude (km s^{-1})	100.83 ± 0.09
Sec. $v \sin i$ (km s^{-1})	38.0 ± 2.0
V_γ (km s^{-1})	19.19 ± 0.10
E[$B-V$] (mag)	0.060 ± 0.005
Sec. log g (dex)	4.39 ± 0.02
Sec. Z (dex)	-0.14 ± 0.05
Sec. $T_{\rm eff}$ (K)	5950 ± 30
Sec. radii ($R_\odot$)	1.06 ± 0.01
Sec. mass ($M_\odot$)	1.0 ± 0.05
WD mass ($M_\odot$)	0.87 ± 0.06
WD $T_{\rm eff}$ (K)	24605 ± 800
WD log g (dex)	8.4 ± 0.1
WD radii ($R_\odot$)	0.01004 ± 0.0008
WD cooling age (Myr)	7.86 ± 0.14

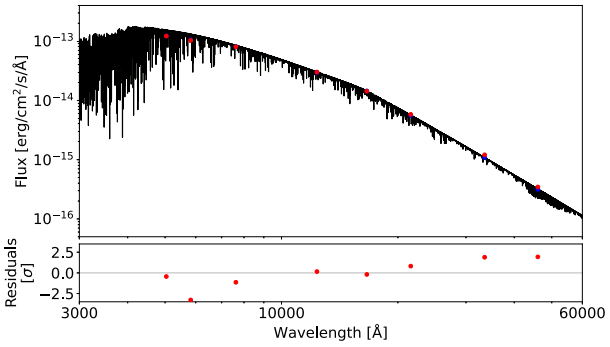

Figure 3. SEDs created from $G_{\rm BP}$, $G_{\rm RP}$, and *G Gaia* bands, *J*, *H*, and K_s band data from 2MASS, and *W*1 and *W*2 band data from *WISE* (red dots) were fitted with MARCS.GES theoretical spectra (black line).

3.3 The white dwarf

To obtain the white dwarf mass, radius, effective temperature, and surface gravity, we fitted the *HST*/STIS spectrum of CPD-65 264 to a synthetic spectrum of a pure hydrogen atmosphere white dwarf (Koester 2010). To that end, we created a grid of synthetic spectra where the effective temperatures spread from 12 000–30 000 K spaced by steps of 200 K and the surface gravity spans over the range of 6.0–9.0 divided into steps of 0.1, and establishing the mixing length parameter to 0.8. We used the MCMC code provided by the EMCEE python package (Foreman-Mackey et al. 2013), assuming for the reddening and parallax the same priors as for the secondary star (we show the best fit of the spectra in Fig. 4). This procedure provides the surface gravity and the effective temperature of the white dwarf.

To obtain the white dwarf mass and radius, we interpolated cooling models from Bédard et al. (2020). The cut-off in the last 100 steps of the chain allowed us to get the best values of the mass and radius which is nearly independent of the assumed thickness of the atmosphere. We used the marginalized distribution to find the white dwarf

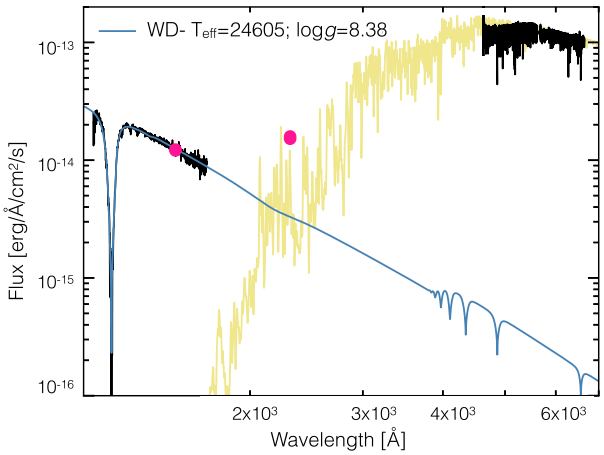

Figure 4. SED of CPD-65 264 covering the ultraviolet and optical wavelength range. We show the observed spectra in black including the ultraviolet *HST* spectrum of the white dwarf and the optical UVES spectrum of the main-sequence star. In yellow, we plot the best MARCS.GES synthetic model of the main-sequence star. The blue line represents the pure-hydrogen synthetic model of the white dwarf. Additionally, we include the *GALEX* near- and far-ultraviolet fluxes as pink dots. The combined flux from the WD models and the main-sequence star model underestimate the *Galex* near-ultraviolet flux. We assume that the model of the G-type secondary star is underpredicting the near-ultraviolet emission as steady chromospheric emission is not taken into account but likely occurring in active G-type stars. We observed the same effect in previously studied systems (Hernandez et al. 2022).

parameters and their statistical errors ($\log g = 8.381 \pm 0.005$ dex, $T_{\rm eff} = 24\,605 \pm 48$ K, $M_{\rm WD} = 0.865 \pm 0.003\,M_\odot$, $R = 0.01004 \pm 0.00004\,R_\odot$, and cooling age of 7.859 ± 0.005 Myr). Furthermore, using the binary mass-function, and the data obtained so far, we deduce the inclination of the system, which is indicated in Table 2.

We note that the above uncertainties of the white dwarf parameters are purely statistical, i.e. systematic errors are not included. The true uncertainties are certainly larger. Barstow et al. (2003) compared log g and $T_{\rm eff}$ derived from analysing the Balmer lines with those deduced from observations of the Ly α line and obtained a relatively large scatter. We very roughly estimate the true uncertainty of the white dwarf mass by assuming an increased uncertainty of 0.1 dex in log g and 800 K in $T_{\rm eff}$ which is broadly consistent with the scatter in Barstow et al. (2003, their figs 9 and 10). With this estimate, we should be on the safe side given that Gianninas, Bergeron & Ruiz (2011) estimate smaller systematic uncertainties typically around 1.5 per cent in $T_{\rm eff}$ and 0.04 dex in log (g) (albeit from fitting optical data). The assumed systematic uncertainties given above translate into more realistic uncertainties of the white dwarf parameters which are listed in Table 2.

4 THE ACTIVE SECONDARY AND THE TESS LIGHT CURVE

Main-sequence stars in close binaries tend to rotate faster than single stars (Rebassa-Mansergas, Schreiber & Gänsicke 2013; Avallone et al. 2022). In post-common envelope binaries, the orbit is circular (e.g. Nebot Gómez-Morán et al. 2011) and tidal forces should quickly synchronize the rotational and orbital period of the secondary star. For periods below 5 d, synchronization should take less than ∼15 Myr (Fleming et al. 2019, their fig. 4). As we shall see, the short orbital period of CPD-65 264 resulted in synchronized rotation despite the

Table 3. Period, amplitude, and starspot coverage derived from the data of the five *TESS* sectors.

Sector	Time range (BJD-2457000)	Period (d)	Normalized amplitude	Spot area (m^2)	Spot surface (per cent)
Original					
S02	1354-1381	1.4188 ± 0.0001	0.0139 ± 0.0005	5.988×10^{16}	11
S03	1385-1406	1.4188 ± 0.0004	0.0131 ± 0.0001	5.639×10^{16}	10
S04	1410-1436	1.3492 ± 0.0002	0.0106 ± 0.0006	4.577×10^{16}	09
S07	1491-1516	1.4188 ± 0.0002	0.0114 ± 0.0003	4.922×10^{16}	19
S11	1601-1623	1.3492 ± 0.0001	0.0240 ± 0.0001	1.057×10^{17}	08
Residuals					
S02	1354-1381	0.6857 ± 0.0007	0.0013 ± 0.0003		
S03	1385-1406	0.6857 ± 0.0004	0.0063 ± 0.0004		
S04	1410-1436	0.6857 ± 0.0003	0.0051 ± 0.0004		
S07	1491-1516	0.6857 ± 0.0005	0.0020 ± 0.0002		
S11	1601-1623	0.6857 ± 0.0008	0.0016 ± 0.0003		

young age of the white dwarf (7.9 Myr) that further confirms that the synchronization time-scale decreases for shorter orbital periods (as expected e.g. from fig. 4 of Fleming et al. 2019).

To investigate the rotation of the secondary star in CPD-65 264, we inspected the high-cadence *TESS* light curves, which we downloaded from the Mikulski Archive for Space Telescopes (MAST)[3] web service. The star was observed in five sectors (hereafter S02, S03, S04, S07, and S11), whose relevant time spans are listed in Table 3.

We extracted the Pre-search Data Conditioned Simple Aperture Photometry (PDCSAP) that removes trends caused by the spacecraft, removed all data points with a non-zero quality flag and all NaN values in each sector. We then analysed each sector with the least-squares spectral method based on the classical Lomb–Scargle periodogram (Lomb 1976; Scargle 1982) to obtain the main period of the photometrical *TESS* data in each sector (see Fig. 5). We found two main periods in the five sectors, 1.4188 d for sectors S02, S03, and S07 while the light curve of sectors S04 and S11 fit better with a period of 1.3493 d. The light curve of each sector phase folded over their corresponding period is shown in Fig. 6. While the photometric periods are similar to the orbital period of the system (1.3701 d), they differ by ∼84.5 and ∼30 min, respectively.

We interpret the photometric periods as being caused by starspots and the small but significant differences to the orbital period as being caused by latitudinal differential rotation, i.e. the photometric period we measure depends on the latitude of the starspots.

Following the method described in Notsu et al. (2019), we estimated the temperature of the starspots and the surface area covered by them. This goes as follows. First, to obtain the temperature of the starspots (T_s), we used equation 4 of Notsu et al. (2019), which is based on the temperature of the main-sequence star ($T_{\rm MS} = 5950$ K):

$T_s = -3.58e^{-5}\, T_{\rm MS}^2 - 0.249\, T_{\rm MS} + 808.0 + T_{\rm MS}$.

We then used the resulting starspot temperature ($T_s \approx 4009$ K) to calculate the area (A_s) that the starspots cover on the surface of the main-sequence star based on the variation of the light curve using equation 3 from Notsu et al. (2019): $A_s = 2\pi R_{\rm MS}^2 \frac{\delta F}{F} \left(1 - \left(\frac{T_s}{T_{\rm MS}}\right)^4\right)^{-1}$.

Here, $\frac{\delta F}{F}$ is the normalized amplitude measured from the phase folded light curve of each sector (see 'original' section of Table 3, e.g. amplitude/flux zero), and $R_{\rm MS}$ is the radius of the star. The total surface covered with starspots varies from 4.577×10^{16} to $1.057 \times 10^{17}\, m^2$, equivalent to 8–19 per cent of the total surface. These values correspond to a relatively small spot coverage for solar-type stars with rotational periods between 0.24 and 11.16 d which spans from 1×10^{15} to 1×10^{18} m^2 (Doyle, Ramsay & Doyle 2020).

[3] https://mast.stsci.edu

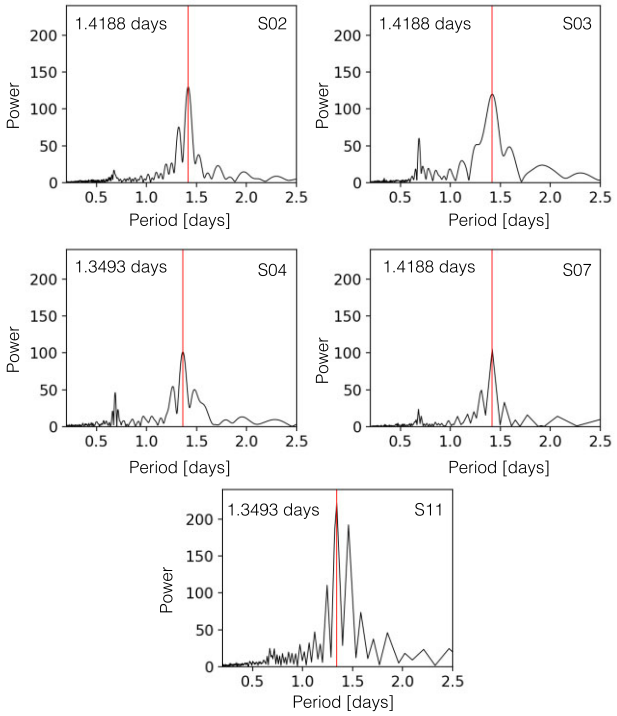

Figure 5. Resulting periodograms of the *TESS* light curves for each sector. Sectors are specified on the upper right corner of each panel, the red line shows the main period identified in each sector (see the periods and errors in Table 3).

The left-hand panel of Fig. 7 shows the unfolded *TESS* light curve which illustrates that short-term variations in shape and amplitude are present in each sector. This confirms that the area and/or number of starspots on the surface of the main-sequence star significantly vary with time. The average area covered by starspots for each sector is given in Table 3.

Looking carefully at the periodograms in Fig. 5, we identify one signal at half orbital period (0.6857 d) in all five sectors. To further investigate the origin of this periodic signal, we removed the main

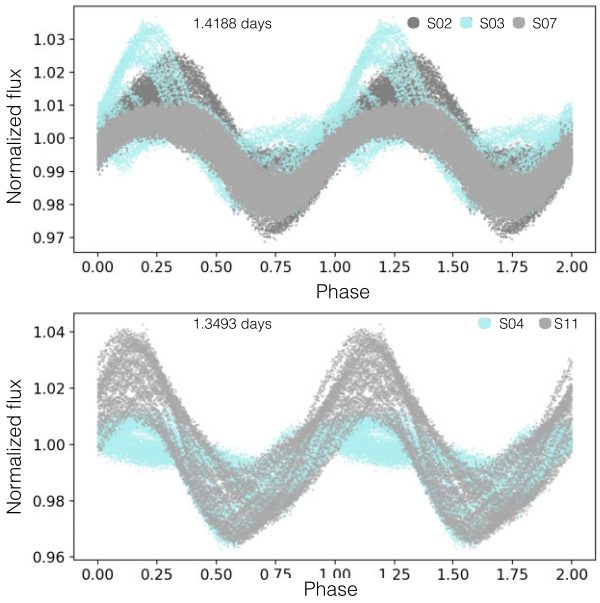

Figure 6. *TESS* light curves of CPD-65 264, two different periods were detected in the five sectors. The upper panel shows the light curves of sectors S02 (dark grey), S03 (blue), and S07 (light grey) phase folded over 1.4188 d. The bottom panel shows sectors S04 (blue) and S11 (light grey) phase folded over the period of 1.3494 d. All light curves used the same phase zero shown in Table 2 to align with the radial velocity curve. The disagreement between the two photometric periods and the orbital period suggests that the G-type star is rotating differentially, i.e. the period we measure depends on the latitude of the starspots dominating the flux variations.

dominant photometric periods with their alias from each sector and then phase folded the residuals over half the orbital period (0.6857 d).

An obvious interpretation for the signal at half the orbital period is ellipsoidal variations. According to Morris & Naftilan (1993) and Zucker, Mazeh & Alexander (2007), the expected amplitude of ellipsoidal variations can be estimated using the following equation:

$$\frac{\delta F}{F} = 0.15 \frac{(15 + u_{\rm MS})(1 + \beta_{\rm MS})}{(3 - u_{\rm MS})} \left(\frac{R_{\rm MS}}{a}\right)^3 q \sin^2 i, \quad (1)$$

where $\frac{\delta F}{F}$ is the fractional semi-amplitude of the ellipsoidal variation, $R_{\rm MS}$ is the main sequence star radius, a the semimajor axis, $q = M_{WD}/M_{MS}$ the mass ratio, and i the inclination. For CPD-65 264, these values are given in Table 2. The linear limb darkening coefficient ($u_{\rm MS}$) and the gravity darkening exponent ($\beta_{\rm MS}$) were obtained from tables 24 and 29[4] reported by Claret (2017).

The amplitudes predicted by equation (1) range from 0.00240 to 0.00372 while the measured normalized amplitude form the residual light curves fluctuate between 0.00132 and 0.00641 in the five sectors (specific values for each sector can be found in 'residuals' section of Table 3). While sectors S02, S07, and S11 are in a good agreement with the theoretical prediction, in sectors S03 and S04 the amplitude exceeds what is expected from ellipsoidal variations.

This difference is likely produced by a combination of starspot signals and ellipsoidal variations in sectors S03 and S04. The left-hand panel of Fig. 7 shows the (not phase folded) *TESS* light curve for the five sectors. The second part of the *TESS* light curve of sectors S03 and S04 is quite irregular and shows a double peak which we interpret as being caused by a starspots arising at nearly opposite sides of the star which boosts the signal at half the orbital period (right-hand panel of Fig. 7) by up to 56 per cent.

[4]https://cdsarc.cds.unistra.fr/viz-bin/cat/J/A + A/600/A30#/browse

5 PAST AND FUTURE OF CPD-65 264

With the stellar masses and the orbital period at hand, it is possible to reconstruct the past evolution of the system, thereby providing constraints on theories of close compact binary formation.

Using our own tool that combines the stellar evolution code (SSE; Hurley, Pols & Tout 2000) with the common envelope energy equations as described in Zorotovic et al. (2010) and Roche geometry, we can obtain the range of possible values for the common envelope efficiency ($\alpha_{\rm CE}$). The algorithm is described in detail in Hernandez et al. (2021, see their section 4.1). We allowed $\alpha_{\rm CE}$ to take any value in the range of 0–1 and assumed that the change in orbital energy is the only source of energy available to expel the envelope.

Fig. 8 shows, from top to bottom, the allowed solutions for the total age of the system (i.e. time since the binary was born until the common envelope phase + cooling age of the white dwarf), the initial mass of the white dwarf's progenitor, and the period at the onset of common envelope evolution, as a function of the common envelope efficiency. We distinguish those solutions that are consistent with the small error estimated for the white dwarf mass (0.003 $M_\odot$, dark grey) and solutions allowing the error to be slightly larger (0.06 $M_\odot$, light grey). In both cases, we found reasonable solutions with a large range of $\alpha_{\rm CE}$ and without the need of any extra source of energy, which is consistent with the results we found for all similar systems previously characterized by our survey (Parsons et al. 2015; Hernandez et al. 2021, 2022). The breaks observed in the solutions correspond to possible progenitors on different evolutionary stages. Smaller values of $\alpha_{\rm CE} \simeq 0.2$–0.4, consistent with the results obtained for post-common envelope binaries with M-dwarf and brown dwarf companions (Zorotovic et al. 2010; Zorotovic & Schreiber 2022), imply a more massive progenitor ($\sim 4.1\ M_\odot$) that evolved faster and filled its Roche lobe on the thermally pulsating asymptotic giant branch, where the envelope is more extended and therefore less bound. The initial orbital period in this case should have been larger than ~1000 d. On the other hand, for larger efficiencies ($\alpha_{\rm CE} \simeq 0.4$–1.0) the progenitor should have been slightly less massive ($\sim 3.8\ M_\odot$) and filled its Roche lobe on the early asymptotic giant branch, in a binary with initial orbital period in the range of ~210–1000 d.

In any case, the formation of CPD-65 264 can be fully understood by considering only orbital energy during common envelope evolution and by assuming low common envelope efficiencies of 0.2–0.4 in agreement with previous findings for post-common envelope binaries with lower mass secondary stars (Zorotovic et al. 2010; Zorotovic & Schreiber 2022). This is particularly interesting given the relatively large white dwarf mass of CPD-65 264 (0.86 $M_\odot$). To illustrate this, we calculated the maximum orbital period predicted for post-common envelope binaries assuming that the envelope is expelled only through orbital energy. The procedure is based on the reconstruction algorithm from Zorotovic, Schreiber & Gänsicke (2011) and described in detail in Rebassa-Mansergas et al. (2012a). In short, we assumed that the white dwarf mass is equal to the core mass of the giant progenitor at the onset of mass transfer and that the secondary star mass remains constant during common envelope evolution. A grid of stellar evolution tracks calculated with the SSE code from Hurley et al. (2000), then provides all possible progenitor masses and their radii. The latter must have been equal to the Roche radius at the onset of common envelope evolution that leaves as the remaining free parameters the final orbital period and

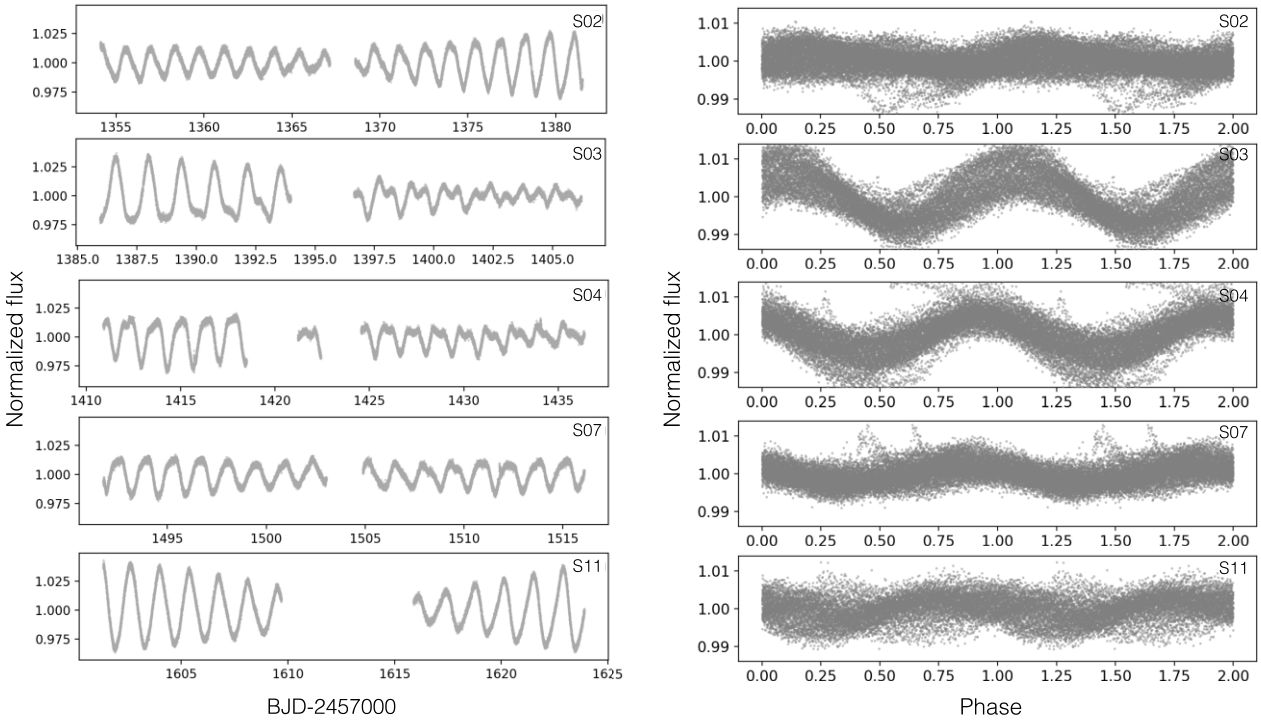

Figure 7. *Left*: The *TESS* light curve of CPD-65 264 detailing the magnetic variability of the main-sequence star throughout changing spot structures. *Right*: Variation detected in the *TESS* light curves after removing their main photometrical signal according to each sector. All five sectors are phase folded over the same period (0.6857 d) corresponding to the half spectroscopic period and with the same phase zero (Table 2). The variation is consistent with arising from ellipsoidal variations in sectors S02, S07, and S011 while in the other two sectors contributions from star spots at roughly opposite sides of the secondary need to be assumed. Each panel corresponds to the sector marked in the upper right corner.

the common envelope efficiency. Assuming the maximum common envelope efficiency then provides the longest possible final orbital period as a function of white dwarf and secondary mass.

As shown in Fig. 9, the identification of post-common envelope binaries with orbital periods exceeding 4 d and white dwarf masses exceeding $\sim$0.8 $M_\odot$ would provide evidence for additional energy sources to play a role during common envelope evolution. The fact that the periods we found so far are well below this period limit, in particular in the case of CPD-65 264, indicates that common envelope evolution can usually be understood without assuming additional energy sources. IK Peg remains the only system where assuming only orbital energy fails to reproduce the system parameters we observe today. A second system could be KOI-3278 (Zorotovic et al. 2014) but its lower white dwarf mass and much longer period also move it closer to the period–white dwarf mass relation for stable mass transfer (Rappaport et al. 1995) and it is therefore less clear that this system is indeed a post-common envelope binary. Assuming KOI-3278 is not a PCEB, Fig. 9 could mean that only in the formation of systems with extremely large white dwarf masses, perhaps exceeding 1 $M_\odot$, recombination energy becomes important. Alternatively, IK Peg might just be an outlier that formed through a different yet to be discovered evolutionary channel.

It is also possible to foresee the future evolution of CPD-65 264 by performing simulations with the Modules for Experiments in Stellar Astrophysics (MESA; Paxton et al. 2011). To that end, we assumed as initial parameters those reported in Table 2 and the *star plus point mass with explicit mass transfer rate* module.

We assumed non-conservative mass transfer (setting the parameter $\beta = 1.0$) to start the simulation as nova eruptions should appear as long as the mass transfer stays below the critical values for stable hydrogen burning.

We found that mass transfer should start in 1.53 Gyr from now at an orbital period of 7.7 h. Throughout its evolution, the mass transfer will remain dynamically and thermally stable, the mass of the white dwarf remains constant, and the system evolves as a cataclysmic variable. The secondary becomes fully convective at a period of 3.0 h, when angular momentum loss will switch from being driven by magnetic breaking to being solely caused by gravitational radiation. The binary will reach the minimum orbital period of 1.2 h in 4.78 Gyr, when the secondary star has lost 90 per cent of its mass. Given the mass of the white dwarf and its small cooling age, the system is currently rather young (see Fig. 8) and therefore the secondary will not evolve off the main sequence and be indistinguishable from cataclysmic variables that descend from binaries with less massive secondary stars. The predicted mass transfer rate of CPD-65 264 is shown in Fig. 10.

6 CONCLUSIONS

We present a detailed characterization of CPD-65 264, the seventh system that clearly is a post-common envelope binary with intermediate-mass secondary (Parsons et al. 2015; Hernandez et al. 2021, 2022) identified by our survey. We performed optical and *HST* spectroscopy to measure the orbital period and the stellar masses. *TESS* photometry confirmed the orbital period and showed that the secondary star is active and differentially rotating. We found variations in the *TESS* light curve revealing changes in the size and/or number of starspots, covering between 8 and 19 per cent of the effective area of the star that we observe. *TESS* light curves of post-common envelope binaries can therefore in principle be used to study activity in the fast rotation regime.

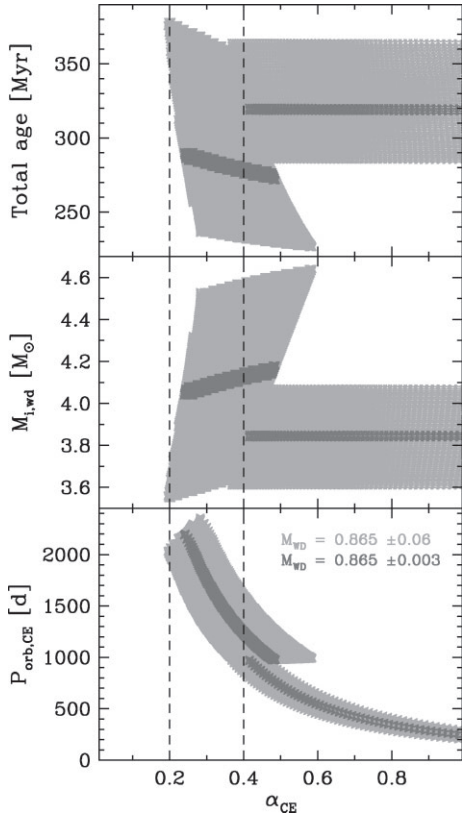

Figure 8. Reconstruction of the past evolution for CPD-65 264 and the possible initial configurations of CPD-65 264 as a function of the common-envelope efficiency α_{CE}. Total age of the system (*top*), initial mass of the progenitor of the white dwarf (*middle*), and orbital period at the onset of the common-envelope phase (*bottom*). The dashed lines demarcate the range of $\alpha_{CE} = 0.2$–0.4 that works for the reconstruction of all the observed post-common envelope binaries with M-dwarf and brown dwarf companions, as well as for the systems previously discovered by our survey.

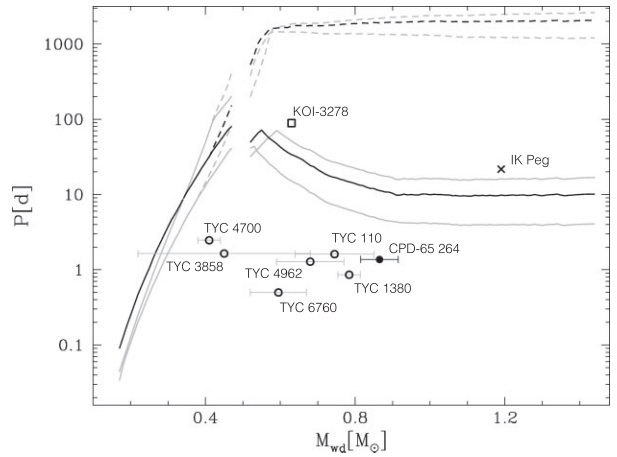

Figure 9. Orbital period limits at which common envelope evolution requires including additional energy sources (solid lines). The limits have been calculated as in Rebassa-Mansergas et al. (2012a) but assuming larger secondary star masses, i.e. 0.5 (lower grey), 1.0 (black), and 1.5 (upper grey) $M_\odot$. The dashed lines indicate the maximum periods if all the available recombination energy contributes to expelling the envelope. IK Peg (the cross) remains the only system whose formation can only be explained by assuming additional energy (e.g. recombination energy) to contribute during common envelope evolution. A second one might be KOI-3278 (square) but it is less clear that this system formed through common envelope evolution. CPD-65 264 is the system with the second largest white dwarf mass but is clearly separated from the critical period that requires additional energy to contribute. This further indicates that the outcome of common envelope evolution can in the vast majority of cases be well understood by considering only orbital energy.

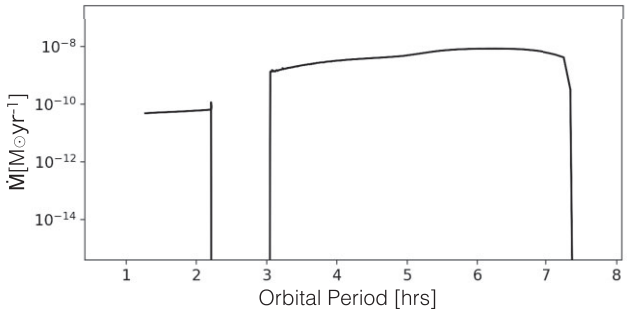

Figure 10. MESA simulation of the future evolution of CPD-65 264. The initial conditions are a white dwarf mass of 0.86 $M_\odot$ and a main-sequence star of 1.0 $M_\odot$ with an orbital period of 1.37 d. In 1.53 Gyr and at an orbital period of 7.7 h, the binary will become a cataclysmic variable, i.e. it will experience (stable) angular momentum loss driven mass transfer. As the secondary will not substantially evolve, the system will detach when magnetic braking is disrupted and evolve as a detached binary through the orbital period gap.

Reconstructing the past and predicting the future evolution of CPD-65 264, we found that the formation of the system can be understood in the context of common envelope evolution without requiring additional energy sources and that in the future the system will become an ordinary cataclysmic variable.

CPD-65 264 further indicates that most observed post-common envelope binaries can be understood as the outcome of common envelope evolution with no extra energy sources and only a small value of the common envelope efficiency. This finding seems to be independent of the mass of the secondary star (Zorotovic et al. 2010; Lagos et al. 2021; Zorotovic & Schreiber 2022).

However, apart from short period post-common envelope binaries, systems with periods exceeding several months that most likely formed through stable and non-conservative mass transfer have been identified (Kawahara et al. 2018), and all systems we identified with periods in between a few days and a few months turned out to be contaminants (Lagos et al. 2022). While we cannot yet draw any final conclusions because the sample sizes are too small, it seems that at least two evolutionary channels are required to understand the population of close white dwarf binaries with intermediate-mass secondary stars. The recently published data release 3 of the *Gaia* mission contains a large number of binary stars with measured orbital periods and it is possible to select candidate binaries with compact objects (Shahaf et al. 2019). Therefore, *Gaia* DR3 may significantly help to identify sufficient numbers of post-mass transfer white dwarf binaries with measured periods to provide solid constraints.

Carefully analysing this potential of *Gaia* DR3 data and eventually comparing a larger sample with the predictions of binary population models will be important for our understanding of white dwarf binaries in general and potentially help to finally understand evolutionary pathways to SN Ia explosions. A first step in this direction has been taken by (Korol, Belokurov & Toonen 2022) who analysed the unresolved double white dwarf population in *Gaia* DR3, a work that should be complemented by studies of their progenitor systems.

ACKNOWLEDGEMENTS

MSH and MRS acknowledge support by ANID – Millennium Science Initiative Program – NCN19_171. MRS and MZ were also supported by FONDECYT (grant 1221059). SGP acknowledges the support of the STFC Ernest Rutherford Fellowship. BTG was supported by the UK STFC grant ST/T000406/1. OT was supported by a Leverhulme Trust Research Project Grant and FONDECYT grant 3210382. ARM acknowledges support from Grant RYC-2016-20254 funded by MCIN/AEI/10.13039/501100011033 and by ESF Investing in your future, and from MINECO under the PID2020-117252GB-I00 grant. RR has received funding from the postdoctoral fellowship programme Beatriu de Pinós, funded by the Secretary of Universities and Research (Government of Catalonia) and by the Horizon 2020 programme of research and innovation of the European Union under the Maria Skłodowska-Curie grant agreement No 801370. For the purpose of open access, the author has applied a creative commons attribution (CC BY) licence to any author accepted manuscript version arising.

DATA AVAILABILITY

Raw and reduced FEROS and UVES data are available through the ESO archive http://archive.eso.org/cms.html.

REFERENCES

Avallone E. A. et al., 2022, ApJ, 930, 7
Barstow M. A., Good S. A., Burleigh M. R., Hubeny I., Holberg J. B., Levan A. J., 2003, MNRAS, 344, 562
Bédard A., Bergeron P., Brassard P., Fontaine G., 2020, ApJ, 901, 93
Bianchi L., 2014, Ap&SS, 354, 103
Blanco-Cuaresma S., Soubiran C., Heiter U., Jofré P., 2014, A&A, 569, A111
Brahm R., Jordán A., Espinoza N., 2017, PASP, 129, 034002
Camacho J., Torres S., García-Berro E., Zorotovic M., Schreiber M. R., Rebassa-Mansergas A., Nebot Gómez-Morán A., Gänsicke B. T., 2014, A&A, 566, A86
Capitanio L., Lallement R., Vergely J. L., Elyajouri M., Monreal-Ibero A., 2017, A&A, 606, A65
Claret A., 2017, A&A, 600, A30
Cutri R. M. et al., 2003, 2MASS All Sky Catalog of point sources. Provided by the SAO/NASA Astrophysics Data System, p. II/246
Cutri R. M. et al., 2012, Explanatory Supplement to the WISE All-Sky Data Release Products, 1
Dekker H., D'Odorico S., Kaufer A., Delabre B., Kotzlowski H., 2000, Design, Construction, and Performance of UVES, the Echelle Spectrograph for the UT2 Kueyen Telescope at the ESO Paranal Observatory. p. 534
Doyle L., Ramsay G., Doyle J. G., 2020, MNRAS, 494, 3596
Fleming D. P., Barnes R., Davenport J. R. A., Luger R., 2019, ApJ, 881, 88
Foreman-Mackey D., Hogg D. W., Lang D., Goodman J., 2013, PASP, 125, 306
Freudling W., Romaniello M., Bramich D. M., Ballester P., Forchi V., García-Dabló C. E., Moehler S., Neeser M. J., 2013, A&A, 559, A96
Gaia Collaboration, 2020, VizieR Online Data Catalog, p. I/350
Gianninas A., Bergeron P., Ruiz M. T., 2011, ApJ, 743, 138
Gustafsson B., Edvardsson B., Eriksson K., Jørgensen U. G., Nordlund Å., Plez B., 2008, A&A, 486, 951
Hernandez M. S. et al., 2021, MNRAS, 501, 1677
Hernandez M. S. et al., 2022, MNRAS, 512, 1843
Hurley J. R., Pols O. R., Tout C. A., 2000, MNRAS, 315, 543
Jordán A. et al., 2014, AJ, 148, 29
Kaufer A., Stahl O., Tubbesing S., Nørregaard P., Avila G., Francois P., Pasquini L., Pizzella A., 1999, Messenger, 95, 8
Kawahara H., Masuda K., MacLeod M., Latham D. W., Bieryla A., Benomar O., 2018, AJ, 155, 144
Kimble R. A. et al., 1998, ApJ, 492, L83
Koester D., 2010, Mem. Soc. Astron. Ital., 81, 921
Kordopatis G. et al., 2013, AJ, 146, 134
Korol V., Rossi E. M., Groot P. J., Nelemans G., Toonen S., Brown A. G. A., 2017, MNRAS, 470, 1894
Korol V., Belokurov V., Toonen S., 2022, MNRAS,515,1228
Lagos F., Schreiber M. R., Zorotovic M., Gänsicke B. T., Ronco M. P., Hamers A. S., 2021, MNRAS, 501, 676
Lagos F., Schreiber M. R., Parsons S. G., Toloza O., Gänsicke B. T., Hernandez M. S., Schmidtobreick L., Belloni D., 2022, MNRAS, 512, 2625
Lallement R., Babusiaux C., Vergely J. L., Katz D., Arenou F., Valette B., Hottier C., Capitanio L., 2019, A&A, 625, A135
Lomb N. R., 1976, Ap&SS, 39, 447
Marsh T. R., 1989, PASP, 101, 1032
Mennekens N., Vanbeveren D., De Greve J. P., De Donder E., 2010, A&A, 515, A89
Morris S. L., Naftilan S. A., 1993, ApJ, 419, 344
Napiwotzki R. et al., 2020, A&A, 638, A131
Nebot Gómez-Morán A. et al., 2011, A&A, 536, A43
Nelemans G., Verbunt F., Yungelson L. R., Portegies Zwart S. F., 2000, A&A, 360, 1011
Notsu Y. et al., 2019, ApJ, 876, 58
Paczynski B., 1976, in Eggleton P., Mitton S., Whelan J., eds, Proc. IAU Symp. 73, Structure and Evolution of Close Binary Systems. Kluwer, Dordrecht, p. 75
Parsons S. G. et al., 2015, MNRAS, 452, 1754
Parsons S. G., Rebassa-Mansergas A., Schreiber M. R., Gänsicke B. T., Zorotovic M., Ren J. J., 2016, MNRAS, 463, 2125
Paxton B., Bildsten L., Dotter A., Herwig F., Lesaffre P., Timmes F., 2011, ApJS, 192, 3
Press W. H., Teukolsky A. A., Vetterling W. T., Flannery B. P., 2007, Numerical Recipes. The Art of Scientific Computing, 3rd edn. University Press, Cambridge
Rappaport S., Podsiadlowski P., Joss P. C., Di Stefano R., Han Z., 1995, MNRAS, 273, 731
Rebassa-Mansergas A., Gänsicke B. T., Schreiber M. R., Koester D., Rodríguez-Gil P., 2010, MNRAS, 402, 620
Rebassa-Mansergas A., Nebot Gómez-Morán A., Schreiber M. R., Gänsicke B. T., Schwope A., Gallardo J., Koester D., 2012a, MNRAS, 419, 806
Rebassa-Mansergas A. et al., 2012b, MNRAS, 423, 320
Rebassa-Mansergas A., Schreiber M. R., Gänsicke B. T., 2013, MNRAS, 429, 3570
Rebassa-Mansergas A., Ren J. J., Parsons S. G., Gänsicke B. T., Schreiber M. R., García-Berro E., Liu X. W., Koester D., 2016, MNRAS, 458, 3808
Rebassa-Mansergas A. et al., 2017, MNRAS, 472, 4193
Ricker G. R. et al., 2015, J. Astron. Telesc. Instrum. Syst., 1, 014003
Scargle J. D., 1982, ApJ, 263, 835
Schreiber M. R., Belloni D., Zorotovic M., Zapata S., Gänsicke B. T., Parsons S. G., 2022, MNRAS, 513, 3090
Shahaf S., Mazeh T., Faigler S., Holl B., 2019, MNRAS, 487, 5610
Sohn S. T. et al., 2019, STIS Data Handbook, Version 7.0. STScI, Baltimore
Webbink R. F., 1984, ApJ, 277, 355
Webbink R. F., 2008, in Milone E. F., Leahy D. A., Hobill D. W., eds, Astrophysics and Space Science Library, Vol. 352, Short-Period Binary Stars: Observations, Analyses, and Results. Springer-Verlag, Berlin, p. 233
Woods T. E., Ivanova N., van der Sluys M. V., Chaichenets S., 2012, ApJ, 744, 12
Zorotovic M., Schreiber M., 2022, MNRAS, 513, 3587
Zorotovic M., Schreiber M. R., Gänsicke B. T., Nebot Gómez-Morán A., 2010, A&A, 520, A86
Zorotovic M., Schreiber M. R., Gänsicke B. T., 2011, A&A, 536, A42
Zorotovic M., Schreiber M. R., García-Berro E., Camacho J., Torres S., Rebassa-Mansergas A., Gänsicke B. T., 2014, A&A, 568, A68
Zucker S., Mazeh T., Alexander T., 2007, ApJ, 670, 1326

This paper has been typeset from a TEX/LATEX file prepared by the author.